Inferring the time-dependent complex Ginzburg-Landau equation from modulus data

Rotha P. Yu, David M. Paganin,* and Michael J. Morgan†
School of Physics, Monash University, Victoria 3800, Australia
(Received 23 December 2004; revised manuscript received 16 August 2005; published 30 November 2005)

We present a formalism for inferring the equation of evolution of a complex wave field that is known to obey an otherwise unspecified (2+1)-dimensional time-dependent complex Ginzburg-Landau equation, given field moduli over various closely spaced planes. The phase of the complex wave field is retrieved via a noninterferometric method, and all terms in the equation of evolution are determined using only the magnitude of the complex wave field. The formalism is tested using simulated data for a generalized nonlinear system with a single-component complex wave field. The method can be generalized to multicomponent complex fields.

DOI: 10.1103/PhysRevE.72.056711 PACS number(s): 05.10.−a, 03.65.Ta, 03.75.Lm, 03.75.Kk

I. INTRODUCTION

Consider a complex quantum-mechanical wave function (or complex order parameter field) appearing in a particular law of physics governing its spatial and temporal evolution. Such equations of evolution are often partial differential equations, such as the linear or nonlinear Schrödinger equations, the Klein-Gordon equation, the Gross-Pitaevskii equation, or the complex Ginzburg-Landau equation. Can such partial differential equations be treated as an unknown, which is to be inferred from measurements of probability density? Such inference of the precise form of the governing partial differential equation involves using modulus data to impose constraints on the equation, a process known as "identification" of the equation of evolution [1,2]. This approach has been limited to real scalar fields or known complex scalar fields (see, e.g., [3–5]). In such cases the equation of evolution of a complex scalar field can only be identified if both the probability density (intensity) and phase of the complex wave field are known *a priori*. However, under the Born interpretation of quantum mechanics, the phase of a complex wave function is not directly measurable. In such a context, we reiterate the fundamental question: can we infer the equation of evolution governing a complex field, given only modulus data?

In attacking this question, an important analytical tool is provided by recent work directed towards noninterferometric determination of the phase of a complex wave field from modulus data, a task commonly termed "phase retrieval" (e.g., [6–8]). However, such an approach assumes a known equation of evolution for the wave field. In a previous paper we demonstrated the feasibility of determining the evolution equation of a complex field, given modulus data alone, assuming the field to obey an otherwise unspecified dissipative (2+1)-dimensional nonlinear Schrödinger equation [9]. Here, we extend this work to a larger class of otherwise unspecified equations of evolution—the (2+1)-dimensional time-dependent complex Ginzburg-Landau equation, one of the most-studied partial differential equations in mathematical physics (see, e.g., [10]). Specifically, we provide a means for "measuring" or inferring an otherwise-unspecified (2+1)-dimensional time-dependent complex Ginzburg-Landau equation from modulus information on a complex field governed by such an equation.

We close this Introduction with an outline of the remainder of the paper. In Sec. II we introduce the time-dependent complex Ginzburg-Landau equation, together with the form of this equation which is obtained via the Madelung transformation. This section also outlines the computational procedures used to numerically evolve the Ginzburg-Landau wave function over a discrete space-time lattice, thereby providing synthetic data for use in later sections of the paper. Section III discusses wave-function phase retrieval in the presence of diffusion by making use of one member of the Madelung-transformed version of the time-dependent complex Ginzburg-Landau equation. Section IV discusses the sensitivity of the retrieved wave-function phase on the error in the diffusion parameter. In Sec. V we apply our formalism for extracting all terms in an otherwise-unspecified (2+1)-dimensional time-dependent complex Ginzburg-Landau equation from simulated modulus data. These modulus data are taken over several closely spaced planes, each of which corresponds to a particular constant value of time. Section VI generalizes our discussion to multicomponent complex fields, Sec. VII discusses the limitations of our numerical scheme, and in Sec. VIII we conclude with a discussion of some implications of this formalism and suggest future directions.

II. TIME-DEPENDENT COMPLEX GINZBURG-LANDAU EQUATION

The time-dependent complex Ginzburg-Landau (TDCGL) equation is

$$\left[i\alpha \frac{\partial}{\partial z} + (1 - i\eta)\nabla_{\perp}^2 + f(I) + ig(I) \right] \Psi = 0, \qquad (1)$$

where $\Psi \equiv \Psi(x,y,z)$ is the complex wave function (or complex order parameter field), $I \equiv I(x,y,z) = |\Psi(x,y,z)|^2$ is the probability density, or the intensity, α and η are real parameters, $f(I)$ and $g(I)$ are real-valued functions of I which, re-

*Electronic address: David.Paganin@sci.monash.edu.au
†Electronic address: Michael.Morgan@sci.monash.edu.au

spectively, quantify the nondissipative and dissipative character of the system, z is the evolution parameter (henceforth taken to be time), and $\nabla_\perp \equiv (\partial/\partial x, \partial/\partial y)$ is the gradient operator in the Cartesian x-y plane. Special cases of the TDCGL equation (1) describe a wide variety of both classical and quantum systems, such as monoenergetic electron beams [11], beamlike monochromatic scalar electromagnetic waves [12], intense scalar electromagnetic fields in nonlinear media [13], Bose-Einstein condensates [14], uncharged superfluids, and vortices and strings in field theory [15].

When we refer to "measuring" or inferring the equation of evolution of a field governed by a differential equation that is a special case of the TDCGL equation (1), we mean the following: solving for all the parameters (α and η), functions [$f(I)$ and $g(I)$], and the phase $\arg(\Psi)$ of the complex scalar field Ψ from given modulus data information I. This modulus information is provided over several closely spaced planes of constant z. By "closely spaced," we refer to the requirement that the evolution of probability density, for any fixed (x,y), vary linearly with z when z lies between the values of any two adjacent measurement planes.

In investigating a means for measuring the TDCGL equation (1), we limit ourselves to simulated modulus data. Our work proceeds in two stages. In the first stage we focus on generating simulated data from the known TDCGL equation (1) [i.e., forward evolution of the wave function Ψ in Eq. (1) with α, η, $f(I)$, and $g(I)$ specified]. The second stage solves for the TDCGL equation (1) based on the assumption that only the modulus information $I=|\Psi|^2$ is known, this modulus information being given over several closely spaced planes of constant z.

In the forward evolution, we solve Eq. (1) using a fourth-order Runge-Kutta differentiation scheme (see, e.g., [8,9,16]). The simulations were performed using a numerical grid with 2025×2025 pixels in x and y, with z step $\Delta z = 10^{-7}$ running for 300 iterations. Numerical data (modulus information and/or the phase) are obtained from a central subset with spatial grid size 1025×1025 within the simulation domain $[0,1]\times[0,1]$, corresponding to spatial step $1/1024$. Our simulations use $\alpha=1$, $\eta=2$, and $f(I) = 100\sin(\pi I)$, with the power dissipation function specified by $g(I)=3I^2$.

The initial condition is based on a Gaussian intensity profile with sinusoidal modulation

$$I(x,y) = A\left\{1+\delta\exp\left[-\frac{1}{2}\left(\frac{r-r_0}{w}\right)^2\right]\cos[2\pi n(x-x_0)]\right\} \times\left\{1+\delta\exp\left[-\frac{1}{2}\left(\frac{r-r_0}{w}\right)^2\right]\sin[2\pi n(y-y_0)]\right\} \times\exp\left[-\frac{1}{2}\left(\frac{r-r_0}{W}\right)^2\right], \tag{2}$$

where A is a constant denoting the peak of the Gaussian profile of width W located at $r=\sqrt{x^2+y^2}=r_0$. We choose $A=10, W=1/8, \delta=0.01, r_0=0.5$, and $n=20$. The initial phase of the system is specified by the Gaussian profile

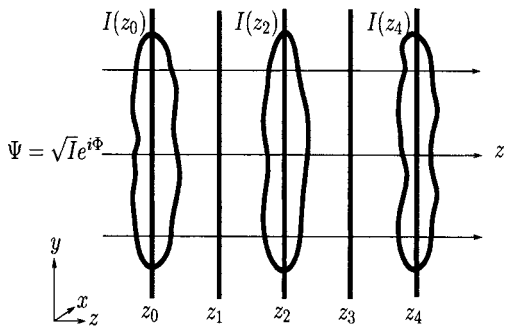

FIG. 1. The evolution of the complex field Ψ as a function of the evolution parameter z. We use the intensity I at various slices $z=z_0$, $z=z_2$, and $z=z_4$ to infer the evolution equation of the system.

$$\Phi(x,y) = A_\Phi\exp\left[-\frac{1}{2}\left(\frac{r-r_0}{W}\right)^2\right], \tag{3}$$

where A_Φ is a constant, which can be used to vary the average phase gradient of the system. We performed simulations with A_Φ in the range [0,2]. Within this range, the average phase gradient $\langle|\nabla_\perp\Phi|\rangle$ is approximately in the range [0,2].

As Ψ evolves through z we output the intensity profile to a file after every 100 iterations. The profile at the 100th iteration corresponds to evolution parameter $z=z_0$, the profile at the 200th iteration corresponds to $z=z_2$, and the profile at the 300th iteration corresponds to $z=z_4$ (see Fig. 1). The phase profile of Ψ is also written to a file at every 100 iterations, for later comparison with the recovered maps of wave-function phase.

Given the measurements of the probability density distribution I of a system over closely spaced planes of fixed z, we solve for the evolution equation of the system. Specifically, given the intensity profiles at z_0, z_2, and z_4, we infer the complex Ginzburg-Landau equation (1). We start by considering the formulation of Eq. (1) in polar coordinates via the Madelung transformation [17]

$$\Psi = \sqrt{I}e^{i\Phi}, \tag{4}$$

where $\Phi=\Phi(x,y,z)$ is the phase of the complex field Ψ. Substituting Eq. (4) into Eq. (1) and, upon separating the real and imaginary components, we obtain two independent equations

$$\frac{1}{I}\nabla_\perp\cdot(I\nabla_\perp\tilde{\Phi}) + \frac{\eta\alpha}{2}|\nabla_\perp\tilde{\Phi}|^2 + G = 0, \tag{5}$$

$$\frac{\partial\tilde{\Phi}}{\partial z} - \frac{\eta}{\alpha}\frac{1}{I}\nabla_\perp\cdot(I\nabla_\perp\tilde{\Phi}) + \frac{1}{2}|\nabla_\perp\tilde{\Phi}|^2 + F = 0, \tag{6}$$

where $\tilde{\Phi}=2\Phi/\alpha$ and

$$G \equiv \frac{1}{I}\frac{\partial I}{\partial z} + \frac{2g(I)}{\alpha} - \frac{2\eta}{\alpha}\frac{1}{\sqrt{I}}\nabla_\perp^2\sqrt{I}, \tag{7}$$

$$F \equiv -\frac{2f(I)}{\alpha^2} - \frac{2}{\alpha^2}\frac{1}{\sqrt{I}}\nabla_\perp^2\sqrt{I}. \tag{8}$$

In this form, Eq. (5) is a diffusion-type equation with diffusion coefficient η/α, whereas Eq. (6) is analogous to the Navier-Stokes equation for an incompressible fluid [15].

Inferring the TDCGL equation involves first solving Eq. (5) for the phase Φ (see, e.g., [9]). This phase retrieval step is treated in the following pair of sections (Secs. III and IV). It is only after this phase-retrieval step has been completed that we perform the subsequent step of equation identification (Sec. V).

III. PHASE RETRIEVAL IN THE PRESENCE OF DIFFUSION

To illustrate the method in which $\tilde{\Phi}$ (or Φ) may be retrieved, we solve Eq. (5) for $\tilde{\Phi}$ assuming for the moment that α, η, I, and $g(I)$ are known. We write Eq. (5) as

$$\nabla_\perp^2\tilde{\Phi} + \frac{1}{I}\boldsymbol{\nabla}_\perp I\cdot\boldsymbol{\nabla}_\perp\tilde{\Phi} = -G - \frac{\eta\alpha}{2}|\boldsymbol{\nabla}_\perp\tilde{\Phi}|^2. \tag{9}$$

The last term on the right-hand side of Eq. (9) may be regarded as a perturbation of second order in the phase gradient. This suggests an iterative numerical scheme to solve for the phase. At the kth iteration Eq. (9) is written as

$$\nabla_\perp^2\tilde{\Phi}_k + \frac{1}{I}\boldsymbol{\nabla}_\perp I\cdot\boldsymbol{\nabla}_\perp\tilde{\Phi}_k = -G - \frac{\eta\alpha}{2}|\boldsymbol{\nabla}_\perp\tilde{\Phi}_{k-1}|^2, \tag{10}$$

where $\tilde{\Phi}_{k-1}$ is the phase at the previous, $(k-1)$th iteration. At the first iteration $(k=1)$ we set $|\boldsymbol{\nabla}_\perp\tilde{\Phi}_0|=0$. At successive iterations, $\tilde{\Phi}_k$—the only unknown in the above nonlinear second-order partial differential equation—is obtained using a multigrid numerical scheme [18], which is implemented via the MUDPACK package [19–21].

The iterative scheme assumes that the phase gradient is small. Therefore a successful and accurate recovery of the phase requires, as a necessary condition for the use of our method, that $|\boldsymbol{\nabla}_\perp\tilde{\Phi}| \lesssim 1$.

The convergence criterion of the iterative numerical scheme is determined by the change in the total phase gradient (the norm of the phase gradient) of the retrieved phase, $\|\boldsymbol{\nabla}_\perp\tilde{\Phi}\|$, over two successive iterations. The scheme is said to converge when $\|\boldsymbol{\nabla}_\perp\tilde{\Phi}\|_k - \|\boldsymbol{\nabla}_\perp\tilde{\Phi}\|_{k-1}$ is small—e.g., less than 10^{-6}.

At every iteration we monitor the root-mean-square (rms) error of the phase gradient, $\sigma(|\boldsymbol{\nabla}_\perp\Phi|)$. This is defined according to

$$\sigma(|\boldsymbol{\nabla}_\perp\Phi|)^2 \equiv \frac{\int_\Omega (|\boldsymbol{\nabla}_\perp\Phi_E| - |\boldsymbol{\nabla}_\perp\Phi|)^2\, dx\, dy}{\int_\Omega |\boldsymbol{\nabla}_\perp\Phi_E|^2\, dx\, dy}, \tag{11}$$

where $\Omega \in \mathbb{R}^2$ and Φ_E is the exact phase. Figure 2(a) shows the rms error for $A_\Phi=1$, where the average phase gradient

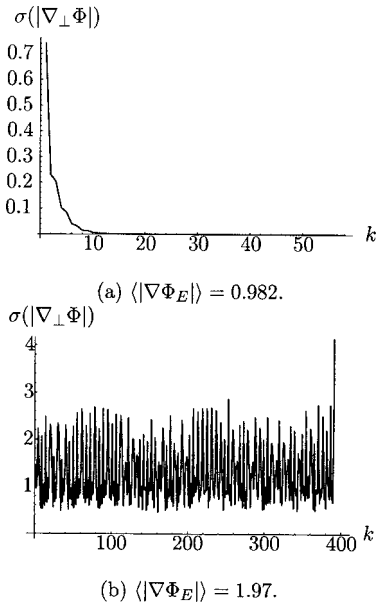

FIG. 2. The rms error of the phase gradient $\sigma(|\boldsymbol{\nabla}_\perp\Phi|)$ as a function of the iteration number k. (a) $A_\Phi=1$ (with $\langle|\boldsymbol{\nabla}\Phi_E|\rangle = 0.982$), showing that the error decreases rapidly and hence the numerical scheme converges. (b) $A_\Phi=2$ (with $\langle|\boldsymbol{\nabla}\Phi_E|\rangle=1.97$). Here the error oscillates, illustrating that the numerical scheme does not converge. After about 390 iterations the error in (b) diverges.

$\langle|\boldsymbol{\nabla}_\perp\Phi_E|\rangle=0.982$; Fig. 2(b) shows the rms error for $A_\Phi=2$, where the average phase gradient $\langle|\boldsymbol{\nabla}_\perp\Phi_E|\rangle=1.97$. The rms error decreases rapidly in (a); however, the error in (b) oscillates and diverges. Numerical simulations show that the numerical scheme converges up to $A_\Phi=1.5$ (i.e., $\langle|\boldsymbol{\nabla}_\perp\Phi_E|\rangle \sim 1.47$); however, the scheme does not converge for $A_\Phi \geqslant 1.6$ (i.e., above $\langle|\boldsymbol{\nabla}_\perp\Phi_E|\rangle \sim 1.57$). This indicates that it is possible to retrieve the phase up to $\langle|\boldsymbol{\nabla}_\perp\Phi_E|\rangle \sim 1.47$, which is well above the constraint imposed by perturbative considerations, i.e., $|\boldsymbol{\nabla}_\perp\Phi_E| \lesssim 1$.

Figure 3(a) shows the retrieved phase for $A_\Phi=0.1$. When one retrieves the phase of a complex wave function governed by a partial differential equation, it is necessary to consider the uniqueness of the retrieved phase. It has been shown by Gureyev *et al.* [22], for the specific case of nondiffusive, nondissipative linear optical systems, that the retrieved phase is unique up to an arbitrary and irrelevant constant. Inclusion of diffusion and dissipation does not alter the conclusion of uniqueness up to an arbitrary additive constant.

Figure 3(b) shows the relative error $\sigma_R(\Phi)$ in the phase, where $\sigma_R(\Phi)$ is defined according to

$$\sigma_R(\Phi) = \frac{\Phi - \Phi_E}{\max(\Phi_E) - \min(\Phi_E)}, \tag{12}$$

where $\max(\Phi_E)-\min(\Phi_E)$ is the range of the exact phase. The error in the retrieved phase at each point (x,y) is measured relative to the range, rather than relative to the value of the exact phase at the point (x,y), since the phase is only measured up to an arbitrary constant. To compare the retrieved phase to the exact phase, we have also shifted both

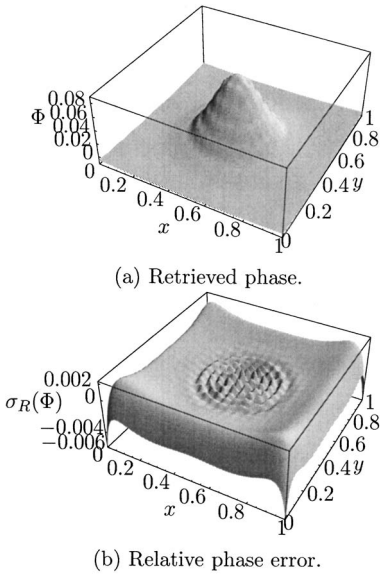

(a) Retrieved phase.

(b) Relative phase error.

FIG. 3. (a) Retrieved phase at z_1 ($A_\Phi=0.1$) and (b) relative error in the phase. The phase is retrieved from the simulated intensity data via the multigrid iterative phase retrieval scheme using the intensity at z_0 and z_2. The relative error in the retrieved phase indicates that phase retrieval is less accurate at the boundary where $I \to 0$; however, the relative error is small in the interior (where I deviates away from zero). This illustrates that it is possible to recover the phase accurately, given modulus information.

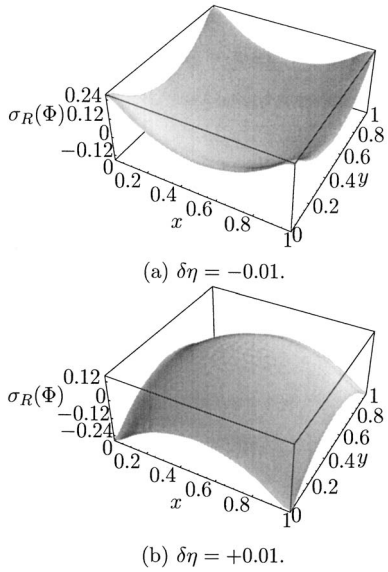

(a) $\delta\eta = -0.01$.

(b) $\delta\eta = +0.01$.

FIG. 4. Relative error in the retrieved phase with various errors in the diffusion parameter η. (a) A negative error in η gives the illusion of "particles" leaving the system, whereas in (b) a positive error in η gives the illusion of "particles" entering the system.

phases so that each has an average of zero. The plot shows that the relative error in the phase is small in the interior and becomes larger at the boundary. This is a consequence of the intensity I approaching zero at the boundary; in this case the phase is not defined. In the interior where the phase is well defined, it can be retrieved with a relative error of less than 1% at most points. The successful and accurate retrieval of the phase in the presence of diffusion is a significant step in our attempt to infer the complex Ginzburg-Landau equation.

IV. PHASE SENSITIVITY WITH ERRORS IN η

The phase-retrieval scheme is robust for a precisely known diffusion parameter η. Here we investigate the effect of an error in η on the retrieved phase.

Figure 4 shows a comparison between the exact phase and the retrieved phase for various errors in η. If we define the boundary of our system, $\partial\Omega$, to be a circle inscribed within the simulation domain $[0,1]\times[0,1]$, it can be seen that the integral N of the normal phase gradient,

$$N \equiv \oint_{\partial\Omega} \nabla_\perp \Phi_E \cdot \mathbf{n}\, dl, \tag{13}$$

where dl is the path along the boundary and $\mathbf{n}$ is an outward-pointing normal to the boundary, of the exact phase approximately vanishes on the boundary. The retrieved phase with a precisely known η [as shown in Fig. 3(a)] is very accurate compared to the exact phase [as shown by the small relative error in Fig. 3(b)]. However, with a negative error in η (i.e., a value of η that is less than its exact value), the quantity N is positive [see Fig. 4(a)]. When the error in η is positive (i.e., a value of η that is greater than its exact value), N is negative [see Fig. 4(b)]. Since $\nabla_\perp \Phi \cdot \mathbf{n}$ is the velocity of the "particles" entering or leaving the system, with $N>0$, Fig. 4(a) gives the illusion of "particles" leaving the system; whereas for $\nabla_\perp \Phi \cdot \mathbf{n} < 0$, Fig. 4(b) gives the illusion of "particles" entering the system. For the situation in which we want to infer the equation of evolution from modulus data, this suggests that accurate inference of the diffusion parameter η is required if we are to infer an equation of evolution that accurately describes the system.

V. INFERRING THE COMPLEX GINZBURG-LANDAU EQUATION

In this section we describe how the TDCGL equation (1) may be solved for the unknown parameters α and η, together with the unknown functions $f(I)$ and $g(I)$ and the phase $\Phi(x,y)$. We divide the task into three parts. In Sec. V A we illustrate how α, η, $\Phi(x,y)$, and $f(I)$ can be determined. This is done by assuming that $g(I)$ is known. In Sec. V B we discuss how $g(I)$ can be determined. Finally in Sec. V C we combine the methods discussed in Secs. V A and V B to infer all the coefficients and functions in the TDCGL equation, given wave-field moduli alone.

A. Inferring α, η, $\Phi(x,y)$, and $f(I)$

The behavior of N due to errors in η allows us to set up a "diffusion relaxation" iteration scheme to accurately infer α, η, $\Phi(x,y)$, and $f(I)$. We do this by assuming *a priori* knowledge of N; that is, we know the total current flowing through the boundary. This *a priori* knowledge of the boundary condition for the phase is not a serious limitation. For example, methods can be developed to measure the phase on

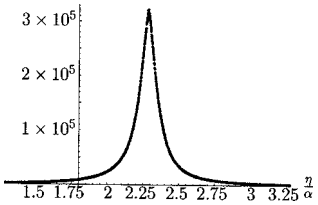

FIG. 5. Frequency histogram of η/α for the case when $\Phi(x,y)=0$. The histogram is constructed from 100 equally spaced isointensity surfaces using Eq. (14). The vertical axis is the number of occurrences of η/α within the interval $\Delta(\eta/\alpha)=10^{-3}$, whereas the horizontal axis shows the various retrieved values of η/α. The value $\eta/\alpha=2.283$ at the peak of the histogram is taken as the initial guessed value of η/α for our diffusion relaxation scheme.

the boundary. One such method was discussed in our previous paper (see [9]). Here, for convenience, we assume $N=0$ on the boundary. This is satisfied, for example, if the system is trapped inside a potential well such as a Bose-Einstein condensate in a harmonic trap [23–25]. It is also satisfied if the system is confined to a container, such as for an uncharged superfluid [26]. In many other finite-size systems, the integrated current density normal to the boundary of the system is expected to be zero (if we choose a boundary that is sufficiently large).

The diffusion relaxation scheme is as follows. In the first iteration we guess η/α. This value is used to retrieve the phase $\tilde{\Phi}$ using Eq. (5) with an arbitrary value of α, which is immaterial since the previous value of $\tilde{\Phi}$ is zero everywhere. Once we have η/α and $\tilde{\Phi}$, we use these quantities to infer α using Eq. (6). We then calculate N on the boundary. If $N<0$, we know that the guessed value of η/α is too large; otherwise, it is too small. We then modify η/α. The initial guess of η/α can take any nonzero value; however, our initial guess is obtained by solving η/α using Eq. (5), with the assumption $\Phi_0(x,y)=0$. We solve for η/α [for the case $\Phi_0(x,y)=0$] in a similar way to how we solved for α in [9]. That is, we substitute pairs of points with the same intensity—i.e., $I_1=I_2$ [where $I_1\equiv I(x_1,y_1,z)$ and $I_2\equiv I(x_2,y_2,z)$]—into Eq. (5) to obtain two independent equations—one equation for each of the points (x_1,y_1) and (x_2,y_2). Subtracting these two equations from one another to eliminate $g(I)$ we obtain

$$\frac{\eta}{\alpha}=\frac{\dfrac{\partial I_1}{\partial z}-\dfrac{\partial I_2}{\partial z}}{2\sqrt{I_1}\nabla_\perp^2\sqrt{I_1}-2\sqrt{I_2}\nabla_\perp^2\sqrt{I_2}}. \tag{14}$$

By using many constant-intensity surfaces a histogram of η/α can be constructed and η/α is obtained as the peak of the histogram (see Fig. 5) [in the specific case when $g(I)$ is known, Eq. (5) may be solved directly for η/α].

To guide us in how to modify η/α at successive iterations, we can guess η/α again at the second iteration. For example, at the second iteration we increase η/α by 1% compared to the value taken by this quantity at the initial guess. This results in N at the second iteration differing slightly from its value at the first iteration. The magnitude and sense in which N varies allows us to systematically modify η/α at subsequent iterations.

The diffusion relaxation scheme is summarized in Appendix A. This scheme fits well with the iterative phase-retrieval method that is used to retrieve the phase of the complex system. For example, at the first iteration α is unknown (even though η/α was approximated or guessed initially). However, it is immaterial since initially we set $\Phi_0(x,y)=0$ and consequently the term $(\eta\alpha I/2)|\nabla_\perp\tilde{\Phi}|^2$ in Eq. (5) vanishes. At successive iterations $(\eta\alpha I/2)|\nabla_\perp\tilde{\Phi}|^2$ is approximated by using α, η, and $\tilde{\Phi}$ from the previous iteration.

In the diffusion relaxation scheme, N at two successive iterations is used to modify η/α at the next iteration. If N at the current iteration has the value $N_k=0$, the normal gradient of the phase $\tilde{\Phi}$ is assumed to be correct and our previous values of α and η are the required solutions. If $N_k\neq 0$, we use the modified diffusion algorithm, given in Appendix A 2, to find the fractional increase, $X_{k+1}=(\eta_{k+1}-\eta_k)/\eta_k$, in η/α. The behavior of the algorithm is as follows.

If N at the current iteration changes from negative to positive (or vice versa)—i.e., $N_kN_{k-1}<0$—it implies that N has overshot (or undershot) the required $N=0$ value. This suggests that the previous value of X is too large and we need to reverse the sign of X. Furthermore, the magnitude of X must be smaller than the previous magnitude; otherwise, N would just undershoot (or overshoot) again with a larger magnitude. To achieve this we modify X according to

$$X_{k+1}=-\frac{N_k}{N_k-N_{k-1}}X_k. \tag{15}$$

The condition $N_kN_{k-1}<0$ guarantees that $|N_k|<|N_k-N_{k-1}|$, and as such we have $|X_{k+1}|<|X_k|$. This condition also guarantees that $N_k/(N_k-N_{k-1})$ is always positive, and thus the sign of X_{k+1} in Eq. (15) is always opposite to X_k.

If N does not change sign between successive iterations—i.e., $N_kN_{k-1}>0$—no overshooting or undershooting occurs. In this situation we compare the magnitude of N at successive iterations. Two possibilities occur, the first of which is $|N_k|>|N_{k-1}|$, with the second being $|N_k|<|N_{k-1}|$ (the situation $|N_k|=|N_{k-1}|$ never occurs as long as $X_k\neq 0$—i.e., $N_{k-1}\neq 0$; otherwise, the algorithm is deemed to have converged). If $|N_k|>|N_{k-1}|$, N diverges. This implies that X_k has the wrong sign. To correct this, we must change the sign of X. We also require that $|X_{k+1}|>|X_k|$; otherwise, there will not be any improvement in N in the next iteration (because a change with $|X_{k+1}|<|X_k|$ is not enough to reverse the previous divergence in N and a change with $|X_{k+1}|=|X_k|$ would just bring N_{k+1} back to N_{k-1} in the next iteration). These requirements can be met by setting

$$X_{k+1}=-\frac{N_k}{N_{k-1}}X_k. \tag{16}$$

That is, since $N_kN_{k-1}>0$ and $|N_k|>|N_{k-1}|$, $|X_{k+1}|>|X_k|$ and the sign of X_{k+1} is always opposite to that of X_k.

However, if $|N_k|<|N_{k-1}|$, $|N_k|$ approaches zero and the iterates converge. In this situation the sign of X_k is correct, and so X_{k+1} should have the same sign as X_k. The magnitude

of X_{k+1} should be proportional to the deviation of N_k from zero. These requirements can be met by setting

$$X_{k+1} = \frac{N_k}{N_{k-1}} X_k. \tag{17}$$

This guarantees that N_{k+1} will converge and the convergence is stable since $|N_k| < |N_{k-1}|$ which always leads to $X_{k+1} < X_k$.

The modified diffusion algorithm in Appendix A 2 guarantees that N always evolves toward zero. The algorithm for obtaining N is analogous to the Newton-Raphson method for finding the root of a nonlinear function [27]. Consequently, the algorithm is robust. At the end of each iteration, we use X to update η/α—i.e.,

$$\left(\frac{\eta}{\alpha}\right)_{k+1} = (1 + X_{k+1})\left(\frac{\eta}{\alpha}\right)_k. \tag{18}$$

The robustness of the diffusion relaxation scheme has been tested numerically. For each iteration, $|X|$ is monitored to test for convergence. If $|X| < \epsilon$, where ϵ is a small tolerance, we consider the numerical scheme to have converged. Since the retrieved phase is sensitive to errors in η in the order of ~ 0.01, the tolerance ϵ is set such that $\eta_{k+1} - \eta_k \ll 0.01$—i.e., $\epsilon = 10^{-7}$. During the iteration scheme η/α, α, and $\tilde{\Phi}$ evolve towards the asymptotic values $(\eta/\alpha)_\infty$, α_∞, and $\tilde{\Phi}_\infty$, respectively.

To ensure that the numerical scheme converges from both sides of $(\eta/\alpha)_\infty$, we reflect the initial guess of η/α through $(\eta/\alpha)_\infty$ and start the iteration scheme again (with the initial values of $\tilde{\Phi}$ reset to zero). The latter numerical scheme converges again, with η/α, α, and $\tilde{\Phi}$ approaching the asymptotic values $(\eta/\alpha)'_\infty$, α'_∞, and $\tilde{\Phi}'_\infty$, respectively, with $(\eta/\alpha)'_\infty \approx (\eta/\alpha)_\infty$, $\alpha'_\infty \approx \alpha_\infty$, and $\tilde{\Phi}'_\infty \approx \tilde{\Phi}_\infty$. The differences between these two sets of asymptotic values are due to the precision of the numerical scheme. Therefore, we take the solutions to be the average of these two sets of asymptotic values.

Figure 6(a) shows the evolution of η as a function of the iteration number k. For an arbitrary guess of η/α, the parameter η can be obtained once we have an approximation for α. The numerical iteration scheme evolves η toward the asymptotic value $\eta = 2.000\,44$. Furthermore, when the initial guess is reflected through the asymptotic value $(\eta/\alpha)_\infty$ (in which case η is also reflected through its asymptotic value) and the iteration scheme rerun, η tends again toward the same asymptotic value. This illustrates that the numerical scheme is robust and η converges quickly. The actual value of η is 2. The error in η may be due to the integral of the normal phase gradient not precisely vanishing on the boundary and from the error in the retrieved phase.

Figure 6(b) shows that α also evolves towards an asymptotic value, $\alpha = 1.007$. When η/α is overestimated, the parameter α evolves towards the asymptotic value from below; however, α is less sensitive when η/α is underestimated. The actual value of α is unity. The error in α may also be due to the error in η/α and the error in the retrieved phase.

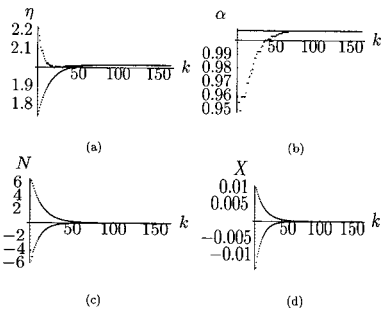

FIG. 6. The evolution of η, α, N, and X in the diffusion relaxation numerical iteration scheme for a typical simulation ($\langle|\Phi|\rangle = 0.49$). (a) η converges to a precise value in the long-term evolution. From above $\eta_+ \to 2.000443$, from below $\eta_- \to 2.000439$. The exact value is $\eta = 2$. (b) When η is overestimated, α was initially underestimated (its exact value is unity); however, it subsequently evolves towards $\alpha_- \to 1.007$. When η is underestimated, α is relatively constant, illustrating that α is less sensitive to a negative error in η when compared to a positive error in this quantity. (c) shows that the normal phase gradient along the boundary tends towards zero from both sides, whereas (d) illustrates the fractional variation of η as it converges towards a solution.

Figure 6(c) shows the behavior of N for $N > 0$ and for $N < 0$. The magnitude of N is large at the start of each iteration. Its values tend towards zero quickly from both sides as a function of iteration number, illustrating the convergence of the numerical scheme. The corresponding fractional change in the diffusion parameter, X, plotted in Fig. 6(d), indicates how η varies during the iterations. The parameter X is varied such that N evolves towards zero and η and α evolve towards their asymptotic values.

A typical frequency histogram of α at the end of the iteration is shown in Fig. 7 ($\langle|\Phi_E|\rangle = 0.49$). The value of α taken from the peak of this histogram is $\alpha = 1.01 \pm 0.04$, with the error taken as the full width at half maximum (FWHM) of the frequency histogram. The relative error in the retrieved phase at the end of the simulation is shown in Fig. 8(a). The profile is typical of the phase being retrieved with positive error in η, consistent with the inferred value of $\eta = 2.000\,44$ (i.e., $\Delta\eta = +0.000\,44$) (see Fig. 4). The magnitude of the relative error is very small, being within 1% at each grid point; this is approximately the relative error that the

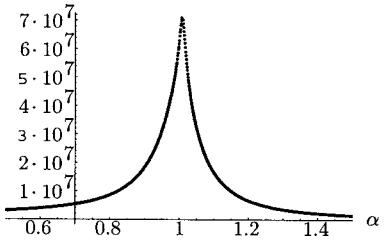

FIG. 7. A typical frequency histogram of α at the end of the diffusion relaxation scheme, for $\alpha = 1.01 \pm 0.04$. The error is taken as the FWHM of the histogram. The histogram is constructed from 100 equally spaced isointensity surfaces using Eq. (6). The vertical axis is the number of occurrences of α within the interval $\Delta\alpha = 10^{-3}$, whereas the horizontal axis shows the various retrieved values of α.

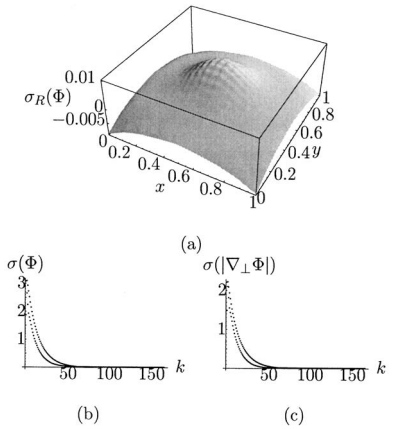

FIG. 8. (a) Relative error in the retrieved phase taken at the end of the diffusion relaxation scheme. This relative error is consistent with an error of η being positive and also consistent with the accuracy with which the phase can be retrieved. (b) and (c) show that the rms error in the phase and the phase gradient quickly decays with increasing iteration number k.

phase can be retrieved with exactly known parameters and functions (see Fig. 2). The fractional rms errors in the phase and in the phase gradient, $\sigma(\Phi)$ and $\sigma(|\nabla_\perp\Phi|)$, are shown in Figs. 8(b) and 8(c). In both cases the fractional rms errors are less than 2%. Note that even when we use the exact values of η and α, the fractional rms errors in the phase and in the phase gradient are also of a similar value.

Once η, α, and Φ are obtained, we can calculate the nonlinear term $f(I)$. This is a straightforward process, which involves the direct application of Eq. (6). A typical result is shown in Fig. 9. Besides a constant energy shift of −131.14 (see [9]), the error in the inferred nonlinear term $f(I)$ is small and can be accounted for from the error in inferring η and α and from the error in the retrieved phase Φ.

So far we have neglected the dissipation term $g(I)$. The diffusion relaxation scheme assumes that the functional form of this dissipation is known. In Sec. V B we discuss the effect of dissipation on the phase of the complex field Ψ, together with ways in which the nonlinear dissipation function $g(I)$ can be inferred.

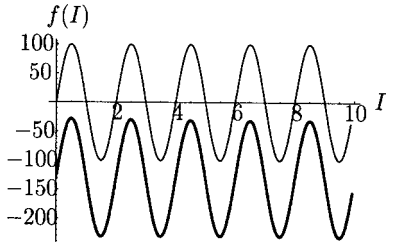

FIG. 9. Comparison between the exact function $f(I)=100\sin(\pi I)$ (upper curve) and the inferred function (lower curve), which can be fitted with $-131.14+100.59\sin(\pi I)$. This illustrates that the nonlinear function $f(I)$ can be recovered accurately. The constant offset is indicative of the fact that the wave-function phase can only be retrieved up to an arbitrary constant.

B. Inferring $g(I)$

Our diffusion relaxation scheme assumes that the dissipation function $g(I)$ is known. In this section we show that, in general, it is hard to solve for the dissipation in the same numerical scheme that is used to infer the parameters η and α and the functions $f(I)$ and Φ [except in the case where $\Phi(x,y,z)=0$]. This is because dissipation has an adverse effect on the evolution of the phase, in the sense that will now be described.

Consider the case when $|\nabla_\perp\tilde{\Phi}|$ is small, for which we can write Eq. (5) as

$$\frac{\partial I}{\partial z}+\nabla_\perp\cdot(I\nabla_\perp\tilde{\Phi})+\frac{2Ig(I)}{\alpha}-\frac{2\eta}{\alpha}\sqrt{I}\nabla_\perp^2\sqrt{I}\approx 0. \quad (19)$$

If we define

$$\nabla_\perp\cdot(I\nabla_\perp H)\equiv\frac{2I}{\alpha}g(I), \quad (20)$$

where $H=H(x,y,z)$ is a real-valued function of position, Eq. (19) may be written as

$$\frac{\partial I}{\partial z}+\nabla_\perp\cdot[I\nabla_\perp(\tilde{\Phi}+H)]-\frac{2\eta}{\alpha}\sqrt{I}\nabla_\perp^2\sqrt{I}\approx 0. \quad (21)$$

Equation (21) is a continuity equation in the presence of a new phase distribution $\tilde{\Phi}+H$. In this equation, the dissipation term completely disappears. Since Eq. (21) is identical to Eq. (19), we see that dissipation modifies the "phase" of the wave function from $\tilde{\Phi}$ to $\tilde{\Phi}+H$ or, equivalently, changes the "flow" velocity by $\nabla_\perp H$. The new current density is $I\nabla_\perp(\tilde{\Phi}+H)$. This implies that dissipation is closely related to the phase of the complex field and one cannot distinguish between the two entities, using the scheme previously outlined.

The phase $\tilde{\Phi}$ can only be determined if H is known or vice versa. Therefore to measure all terms in the TDCGL equation, the dissipation of the system either has to be measured separately or it has to be measured by other means. In [9] we discussed two ways in which the dissipation function $g(I)$ can be measured. Here we generalize these results to include diffusion.

In many systems, such as monoenergetic electron beams or electromagnetic waves, it may be relatively easy to prepare a plane wave state with a constant transverse intensity profile in which the phase $\tilde{\Phi}$ is independent of the x and y positions, over the plane at constant z. Suppose we can prepare the system in such a plane-wave state. In this situation the divergence of the current density $\nabla_\perp\cdot(I\nabla_\perp\tilde{\Phi})$, the second-order velocity field $|\nabla_\perp\tilde{\Phi}|^2$, and the diffraction term $I^{-1/2}\nabla^2\sqrt{I}$ vanishes. Using Eq. (5), the dissipation is then given by

$$\frac{g(I)}{\alpha}=-\frac{1}{2I}\frac{\partial I}{\partial z}. \quad (22)$$

Equation (22) is independent of the diffusion parameter η. This illustrates that for a uniform plane wave, the system

does not diffuse. To obtain the dissipation at different values of the intensity, we need to make repeated measurements. We can separately prepare the system for each of the intensity values, or since the intensity always decreases due to dissipation, we can measure the dissipation over a long-time evolution. For the latter case, we note that the intensity evolves as

$$I(z) = I_0 \exp\left(-\frac{2}{\alpha}\int g(z)dz\right), \tag{23}$$

where I_0 is the intensity at $z=0$, indicating that dissipation leads to decay in the intensity profile of the system.

For nonlinear systems, long-term evolutions of plane-wave states are susceptible to instabilities. A well-known example is the modulational instability of a plane wave. In the absence of dissipation, a plane wave for a nonlinear system is susceptible to modulational instability (see, e.g., [28,29]). Therefore, when measuring dissipation over a long duration, it may be necessary to be cautious of the modulational instability of the plane wave. Here we envisage a scenario in which dissipation is measured and is a monotonic function of the intensity. If the dissipation is measured using a plane wave with large intensity, the dissipation is expected to be large. In such a situation, we would expect the growth of the modulations to be damped out by the dissipation. However, if the measurement is made using a plane wave with small intensity, the dissipation is expected to be small. In this case the dissipation is not sufficient to prevent modulational instability of the plane wave. This may result in inaccurate measurements of the dissipation. In this situation, it may be necessary to monitor the intensity evolution of the plane wave to observe any sign of instability and measurement of the dissipation may only be made over a short duration.

In some systems, such as an uncharged superfluid or a Bose-Einstein condensate, it may be difficult to construct an ideal plane-wave state. Instead, we may produce an approximate plane wave state with some modulations in the intensity and phase. In this case we have a system where $\boldsymbol{\nabla}_\perp I$, $\nabla_\perp^2 I$, and $|\boldsymbol{\nabla}_\perp \tilde{\Phi}|$ are not equal to zero, but are nevertheless small. In this situation we examine an alternative approach to measuring dissipation. As outlined in [9] for the nondiffusive case, an alternative approach is to average the measured dissipation over a large number of measurements, M. For the diffusive case discussed here, when we restrict ourselves to systems with small fluctuations so that $|\nabla_\perp \tilde{\Phi}|$ is small, the second-order term in the velocity field, $|\boldsymbol{\nabla}_\perp \tilde{\Phi}|^2$, is negligible. The continuity equation is then reduced to that given by Eq. (19). The method of averaging discussed in [9] is applicable and the dissipation can be approximated as

$$\left\langle \frac{g(I)}{\alpha} \right\rangle \approx \frac{1}{M}\sum_{m=1}^{M}\left[\frac{\eta}{\alpha}\frac{1}{\sqrt{I}}\boldsymbol{\nabla}_\perp^2\sqrt{I} - \frac{1}{2I}\frac{\partial I}{\partial z}\right]_m, \tag{24}$$

where m denotes the mth measurement and the average is over isointensity surfaces.

In Eq. (24), η/α is not known. The dissipation function should be measured in conjunction with measuring all other parameters and functions in the TDCGL equation (1). The dissipation function may be calculated immediately using Eq. (24) after η/α has been found or approximated at each iteration.

C. Inferring the TDCGL equation

Here we devise a numerical scheme in which all the parameters and functions of the (2+1)-dimensional TDCGL equation can be inferred, given wave-function moduli over closely spaced planes of constant z. Specifically, we implement a method to infer α, η, Φ, $f(I)$, and $g(I)$ in Eq. (1). Our scheme utilizes the numerical methods discussed in Secs. V A and V B.

Suppose we have a set of approximate plane-wave states (i.e., states that are as close to plane-wave states as practicable, where modulation in the amplitude and phase is minimal)

$$P(I_q) = \sqrt{I_q}e^{i\Phi_q}, \tag{25}$$

with the modulated intensity I_q and phase Φ_q $(q=1, 2, \ldots, Q)$ and a noncompact localized state

$$L(I) = \sqrt{I}e^{i\Phi}, \tag{26}$$

with intensity I approaching zero at the boundary and nonvanishing in the interior; here, Φ is the phase of the localized state. The maximum intensity of the localized state, $I_{\max}$, is assumed to be less than or equal to the average intensity of the largest plane-wave state, i.e., $I_{\max} < I_Q$ (where I_Q is the average intensity of the largest plane-wave state).

Once we have the plane-wave states and the noncompact localized state, we devise a numerical scheme to infer the TDCGL equation. Details of the numerical scheme are given in Appendix A 3. The scheme starts by approximating η/α (denoted by $\tilde{\eta}/\alpha$). Similar to Sec. V A, the approximation $\tilde{\eta}/\alpha$ can be found by guessing or via Eq. (14) using one of the plane-wave states at two evolution time-steps. The latter method will be exploited in our numerical simulation. In this case we construct a histogram of $\tilde{\eta}/\alpha$ in a similar manner to that discussed in Sec. V A. The value of $\tilde{\eta}/\alpha$ is taken at the peak of the histogram.

We then employ the approximate value of η/α for computing the dissipation $g(I_q)/\alpha$ for each of the approximated plane-wave states. Since we assume that the approximated plane-wave states have small modulations in the phase, such that $-\eta|\nabla_\perp \Phi|^2/\alpha$ is much smaller compared to the rest of the terms in Eq. (5), this second-order term can be ignored. In this case Eq. (19) can be used as an approximate equation governing the evolution of the intensity I_q of a particular plane-wave state and the dissipation $g(I_q)/\alpha$. Once the dissipation function has been calculated for each of the discrete intensity levels of the plane-wave states, we express it as a continuous function of the intensity variable I. This is accomplished by interpolating the dissipation function between the plane-wave states.

The dissipation for each of the plane-wave states can be computed using the intensity profile I_m at two different evolution times. Long-time evolution of each of the plane-wave states allows us to measure the dissipation over many fluc-

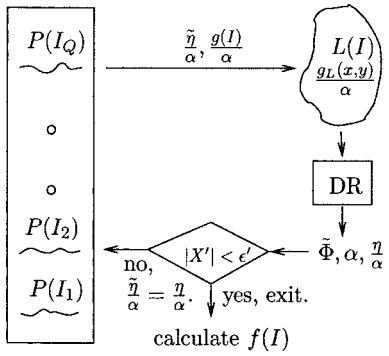

FIG. 10. Schematic illustration of the iteration scheme to infer the TDCGL equation. Multiple modulated plane-wave states $P(I_q)$ and a localized state $L(I)$ are prepared. An initial guess of $\tilde{\eta}/\alpha$ is obtained. The dissipation on the localized state $g_L(x,y)$ is obtained from the dissipation on the plane-wave states $g(I)$ (note that the measurements are in units of α). Given the guess of $\tilde{\eta}/\alpha$ and the approximation for the dissipation, the diffusion relaxation (DR) scheme is used to find $\tilde{\Phi}$, α, and an improved value of η/α. The numerical scheme is repeated if this improved value is not the required stationary value.

tuation cycles. For large samples, these measurements can be used to "wash out" the effect of the fluctuation term $(-1/\alpha I)\boldsymbol{\nabla}_\perp \cdot (I_q \boldsymbol{\nabla}_\perp \Phi_q)$, when the dissipation is averaged over isointensity levels. In such cases we use Eq. (24) to calculate the dissipation; it is expected that for small samples, we would see oscillatory errors in measuring $g(I)/\alpha$ due to ignoring the term $(-1/\alpha I)\boldsymbol{\nabla}_\perp \cdot (I\boldsymbol{\nabla}_\perp \Phi)$, with these errors being dependent on the intensity. Furthermore, since we ignore $-\eta|\boldsymbol{\nabla}_\perp \Phi|^2/\alpha$ when calculating the dissipation, we would also expect an intensity-independent error of $\eta|\boldsymbol{\nabla}_\perp \Phi|^2/\alpha$ in measuring the dissipation.

The continuous intensity-dependent dissipation $g(I)/\alpha$ is then used to calculate the distribution of dissipation, $g_L(x,y)/\alpha$, over the localized state $L(I)$. With the value of η/α and the dissipation known approximately [i.e., by making use of the obtained $\tilde{\eta}/\alpha$ and $g_L(x,y)/\alpha$], we now use the diffusion relaxation (DR) scheme to calculate $\tilde{\Phi}$ and α, and improve on the value of η/α. If the new value of η/α is different from the original value $\tilde{\eta}/\alpha$, we repeat the process by replacing $\tilde{\eta}/\alpha$ with the new η/α. This is as illustrated in Fig. 10. If the improved value of η/α is very close to the value of η/α at the previous iteration, i.e.,

$$X' \equiv \frac{\left| \frac{\eta}{\alpha} - \frac{\tilde{\eta}}{\alpha} \right|}{\frac{\tilde{\eta}}{\alpha}} < \epsilon' = 10^{-7}, \tag{27}$$

we exit the iteration and calculate the function $f(I)$. This is achieved by using Eq. (6), where all other terms are now known [i.e., $\Phi(x,y,z)$, α, and η].

Here we give a specific numerical example to illustrate the implementation of the numerical scheme described above. Numerical simulations use a smaller grid size of 713×713 pixels, and only numerical data (i.e., modulus information) are obtained from a central grid of size 513×513 within the simulation domain $[0,1] \times [0,1]$, corresponding to the spatial step $1/512$ (note that the simulations in this section are at a lower spatial resolution than in the previous sections). Other simulation parameters, if not specified, are as described in Sec. II. The noncompact localized state $L(I)$ is equal to Ψ as defined in Sec. II. For the approximated plane-wave states, we introduce sinusoidal modulations in the ideal plane-wave solution of constant intensity and zero phase. That is, the approximated plane-wave states are specified by Eq. (25) with intensity, I_q and the phases of the plane-wave states Φ_P are given by

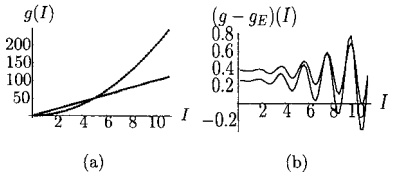

FIG. 11. (a) Dotted points are the measured dissipation and continuous curves are the exact dissipation. These plots show that the dissipation can be inferred very accurately. (b) The error in the dissipation function, $g(I) - g_E(I)$ [where $g(I)$ is the measured dissipation and $g_E(I)$ is the exact dissipation], for the case $g_E(I) = 10I$. The top curve is the error in the measured dissipation in the first measurement, and the bottom curve is the error at the third measurement. The lower error at the third measurement illustrates convergence of the numerical dissipation measurement scheme.

$$I_q = A_q[1 + \delta_I \cos(2\pi n x) + \delta_I \sin(2\pi n y)], \tag{28}$$

$$\Phi_P = \delta_\Phi \cos(2\pi n x) + \delta_\Phi \sin(2\pi n y), \tag{29}$$

where A_q is the nonperturbed intensity at the q-plane wave and n is the wave number. For simplicity the wave number for the intensity is set to have the same value as that for the phase. Furthermore, we also set each of the plane-wave states to have the same modulation. A typical numerical simulation was carried out for $\delta_I = \delta_\Phi = 0.01$, $n = 20$ with A_q in the range $[0.2,12]$ in steps of 0.2, which generates 60 plane waves. Each plane wave is run for 1000 iterations, corresponding to a duration of 10^{-4} (i.e., a time step of 10^{-7}), where intensity data are recorded for each 100 iterations. This resulted in 10 intensity data files and allows us to make nine measurements of the dissipation $g(I_q)/\alpha$ for each of the plane-wave states.

In this section numerical simulations are performed for two types of dissipation, the first being $g_E(I) = 10I$ and the second taken as $g_E(I) = 2I^2$ [where $g_E(I)$ is the exact dissipation function]. The numerical scheme (see Fig. 10) is robust and converges in four iterations. Figure 11(a) shows the measurements of the dissipation (these appear as points) compared to the original dissipation (plotted as solid curves), with one data set for the case $g_E(I) = 10I$ and another for the case $g_E(I) = 2I^2$. For the former set, the measured data can be fitted with the function $g(I) = 10.17I^{0.99}$. The measured data and the fitted data correspond to rms errors of about 0.5% compared to the exact input dissipation $g_E(I) = 10I$. For the latter case, the measured data can be fitted with the function

$g(I)=2.04I^{1.99}$. The measured data and the fitted data for this latter case correspond to rms errors of about 0.3% compared to the exact input dissipation function $g_E(I)=10I$. Furthermore, as can be seen in Fig. 11(a), the measured dissipation data lie on the curves of the exact dissipation functions. This illustrates that the dissipation function can be measured accurately. In Fig. 11(b), the differences between the measured dissipation and the exact dissipation are plotted for the case $g(I)=10I$. The top curve uses the dissipation from the first iteration, and the bottom curve uses the dissipation at the last iteration (the fourth iteration). Small values in the errors in the measured dissipation at the last iteration compared to that at the first iteration indicate that the numerical scheme converges; the very low number of iterations indicates that the convergence is robust.

Figure 11(b) also indicates that there are two types of errors in the dissipation measurements. One is a constant error independent of the intensity, while the second type of error exhibits oscillatory behavior that is dependent on the intensity. The intensity-independent error arises from neglecting the term $\eta|\nabla_\perp\Phi|^2/\alpha$ in Eq. (24). For the specific modulation of the plane-wave phase in Eq. (29), we have $\eta|\nabla_\perp\Phi|^2/\alpha=4\eta\pi^2n^2\delta_\Phi^2/\alpha\approx 3.2$ (based on $\eta/\alpha=2$, $n=20$, and $\delta_\Phi=0.1$) at the beginning of the simulations. The errors in Fig. 11(b) are smaller than this initial value due to damping of the phase gradient as a result of dissipation. This suggests that dissipation has a positive effect on the measurement of dissipation function and may prevent the occurrence of modulational instability as is often the case for a plane wave in a nonlinear system. The intensity independence of this error suggests that if we know that the modulations are the same for each plane-wave state, we can remove the error in the dissipation arising from the term $\eta|\nabla_\perp\Phi|^2/\alpha$ by extrapolating the measured dissipation to zero intensity. Here we assume a monotonic dissipation in which $g(I)\to 0$ as $I\to 0$. Similarly, the errors in the oscillations of the fluctuation term $\nabla_\perp\cdot(I\nabla_\perp\Phi)/(\alpha I)$ can be shown to be in the range $[-4\pi^2n^2\delta_\Phi, 4\pi^2n^2\delta_\Phi]/\alpha\approx[-158,158]$ (based on $\alpha=1$, $n=20$, and $\delta_\Phi=0.01$). The "fluctuation term" errors in Fig. 11(b) are nowhere near the predicted values due to the isointensity averaging methods used in computing the dissipation and the damping effect of the dissipation.

At the end of the simulation η/α evolves toward 1.9989, at which $\alpha\to 1.0080$ [$g_E(I)=10I$]. The phase also can be retrieved very accurately [the retrieved phase is similar to that in Fig. 3(a), whereas the relative error in the phase is similar to that shown in Fig. 4(a)]. The rms error in the retrieved phase is about 2% compared to the exact phase; the rms error in the phase gradient is about 1% compared to the exact phase gradient. At the end of the simulation the values of η/α, α, and the retrieved phases are used to calculate the nonlinear nondissipative interaction $f(I)$ using Eq. (6). Figure 12(a) shows a typical measurement of $f(I)$ compared to the exact $f_E(I)$ [based on a simulation with $g_E(I)=10I$]. The measured function can be fitted with $f(I)=-132.45+100.45\sin(\pi I)$ [see Fig. 12(b)], compared with the exact function $f_E(I)=100\sin(\pi I)$ (neglecting the constant part), indicating that the measurement is accurate. The rms errors in the measured data are 2%, whereas the rms errors in the fitted function are 0.5% compared to the exact function. It is expected that the accuracy will improve given higher spatial resolution, for which η/α, α, and the phase Φ can be retrieved more accurately.

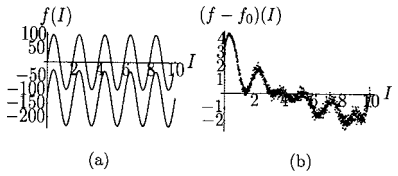

FIG. 12. (a) Measured $f(I)$ (bottom) compared to the exact $f_E(I)=100\sin(\pi I)$ [for the case $g_E(I)=10I$]. The measured $f(I)$ can be fitted with a function $f(I)=-132.45+100.45\sin(\pi I)$, and the small error (neglecting the constant offset -132.45) indicates accurate measurement of the function. (b) The error in measuring $f(I)$; most errors are within 2% and are expected to decrease if simulations are performed at higher spatial resolution.

VI. GENERALIZATION TO MULTICOMPONENT COMPLEX FIELDS

The diffusion relaxation algorithm for inferring the TDCGL equation may be generalized to the case of multicomponent (2+1)-dimensional complex fields, denoted by $\{\Psi_n(x,y,z)\}$, which comprise a set of N complex fields $\Psi_n\equiv\Psi_n(x,y,z)$, $n=1,\ldots,N$. The TDCGL equation governing the evolution of this multicomponent complex field may be written as

$$\left[i\alpha_n\frac{\partial}{\partial z}+(1-i\eta_n)\nabla_\perp^2+f_n+ig_n\right]\Psi_n=0, \tag{30}$$

where α_n and η_n are real numbers, while $f_n(I_1,\ldots,I_N)$ and $g_n(I_1,\ldots,I_N)$ are real-valued functionals dependent on the intensity $I_n=|\Psi_n|^2$. The formulation of Eq. (30) in polar coordinates is

$$\frac{1}{I_n}\nabla_\perp\cdot(I_n\nabla_\perp\tilde{\Phi}_n)+\frac{\eta_n\alpha_n}{2}|\nabla_\perp\tilde{\Phi}_n|^2+G_n=0, \tag{31}$$

$$\frac{\partial\tilde{\Phi}_n}{\partial z}-\frac{\eta_n}{\alpha_n}\frac{1}{I_n}\nabla_\perp\cdot(I_n\nabla_\perp\tilde{\Phi}_n)+\frac{1}{2}|\nabla_\perp\tilde{\Phi}_n|^2+F_n=0, \tag{32}$$

where $\tilde{\Phi}_n=2\arg(\Psi_n)/\alpha_n$ and

$$G_n\equiv\frac{1}{I_n}\frac{\partial I_n}{\partial z}+\frac{2g_n}{\alpha_n}-\frac{2\eta_n}{\alpha_n}\frac{1}{\sqrt{I_n}}\nabla_\perp^2\sqrt{I_n}, \tag{33}$$

$$F_n\equiv-\frac{2f_n}{\alpha_n^2}-\frac{2}{\alpha_n^2}\frac{1}{\sqrt{I_n}}\nabla_\perp^2\sqrt{I_n}. \tag{34}$$

Given modulus information on three closely spaced planes, Eq. (31) may be used to solve for η_n/α_n and $\tilde{\Phi}_n$, using the diffusion relaxation iteration scheme, separately for each component. However, to solve Eq. (32) for α_n, our technique is to find pairs of points with the same f_n. For a single-component complex field, such pairs of points can be found

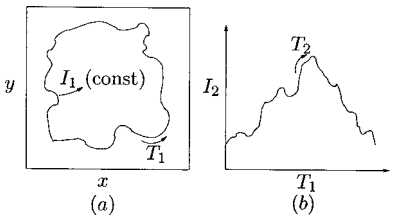

FIG. 13. Schematic illustration of the trajectories T_1 and T_2 corresponding to a path in I_1 and I_2 space. (a) T_1 traverses a path in physical space corresponding to an isointensity surface in I_1. (b) Along the same trajectory in physical space, the intensity I_2 varies in T_2, with the end points identified. In general, the trajectory T_2 is not an isointensity surface; however, there are pairs of points with the same intensity.

on isointensity surfaces. However, this is not always the case for multicomponent complex fields. For arbitrary multicomponent complex fields it is not known how such pairs of points can be found (although such pairs of points exist since f_n vanishes on the boundary and is nonvanishing in the interior). We outlined in [9] that, in principle, for two-component complex fields ($N=2$) in two spatial dimensions, we can always find such pairs of points. Our finding in [9] is also applicable to the TDCGL equation considered in this paper. Here we generalize the arguments for finding pairs of points with the same f_n for two-component complex fields ($N=2$) in two spatial dimensions. We construct a closed trajectory, T_n ($n=1$, say), in which I_1 is an isointensity surface [see Fig. 13(a)]. As we traverse a path in T_1, I_2 traverses the corresponding path in T_2 as shown in Fig. 13(b), where not every point on T_2 necessarily has the same intensity. However, since T_1 is a closed trajectory, T_2 is necessarily a closed trajectory; i.e., the two end points of trajectory T_2 in Fig. 13(b) are identified. Consequently there are at least two points in T_2 with the same intensity, and it is easy to follow the methods developed in this paper to infer the TDCGL equation of the two-component field. This argument can be generalized to infer the TDCGL equation for a three-component complex field in three spatial dimensions. In three spatial dimensions, it is possible to construct a closed isointensity surface T_1 for I_1. For some paths in T_1, it is possible to trace out a closed isointensity loop T_2 for I_2, and for some points in T_2, it is possible to find pairs of points with the same intensity for I_3. Therefore in three spatial dimensions, it is possible to infer the TDCGL equation for a three-component complex field.

VII. LIMITATIONS OF OUR NUMERICAL SCHEME

The main results of this paper are the inference of the TDCGL equation from modulus information. To achieve this we have invoked multiple plane-wave states to infer the dissipative interactions $g(I)$ and a diffusion relaxation scheme acting on a noncompact localized state to infer α, η, and the phase Φ, in which case the nondissipative interactions $f(I)$ can be directly calculated. Notwithstanding the success and robustness of the numerical scheme, there are limitations on the general applicability of the scheme.

When calculating the dissipation, it is obvious that the dissipation would be precisely calculated if we have ideal multiple plane-wave states, for which $\nabla_\perp I_m = \nabla_\perp \Phi_m = 0$, and in the limit where we have an infinite number of plane waves that span the required intensity spectrum. In the absence of the ideal situation, where there are fluctuations in the plane wave, one can minimize the error in measuring the dissipation by evolving the plane-wave states over many cycles of fluctuating oscillations. In the case when the dissipation is weak, averaging the dissipation at the isointensity level, over all the measurements, is expected to "wash out" the errors in the dissipation arising from fluctuations. When the dissipation is large, the fluctuation is expected to damp out over each successive cycle of oscillation. In such a case it may be better to obtain the dissipation from the last two intensity measurements at the end of the evolution, where fluctuations are minimal.

The phase gradient $\nabla_\perp \Phi$ also gives rise to errors in the dissipation measurement in the form of the unknown term $-\eta|\nabla_\perp \Phi|^2/\alpha$. If the fluctuations are sufficiently large (in such a case our system may be very far from the ideal plane-wave state), so that $-\eta|\nabla_\perp \Phi|^2/\alpha$ cannot be ignored, dissipation may not be accurately measured. However, in the latter case, since $-\eta|\nabla_\perp \Phi|^2/\alpha$ is independent of intensity, this error in the dissipation measurement can be removed if we know that the average magnitude of the fluctuations is the same in each of the plane waves (see Sec. V C).

For the diffusion relaxation scheme, our analysis is restricted to localized systems where the intensity I approaches zero (but is not equal to zero; otherwise, the phase cannot be determined) on the boundary. Although we are not considering general nonlocalized systems, there is no reason why the diffusion relaxation method is not generalizable to nonlocalized systems. Notwithstanding this, however, there are situations where the method is suitable. The method is based on the deviation of N from the known zero value on the boundary with respect to the error in the value of η/α. As can be seen in Figs. 4 and 8(a) the deviation in N becomes large in the limit of vanishing I at the boundary. This leads to a very small error in η/α and a large error in N. Since the numerical method is based on minimizing the error in the value of N, this is more accurate in measuring η/α as $I \to 0$ on the boundary. This suggests that the method is suitable for localized systems where I is large in the interior and vanishes on the boundary.

Note that for the case where $I=0$ on the boundary (i.e., compact support), the phase is not determined on the boundary and the numerical scheme is not applicable. Furthermore, it does not make sense to speak of normal current density on the boundary. In this situation, it is trivial to redefine the "boundary" so that the new boundary "sits" at a small, but nonvanishing intensity.

We also only discussed the case where the normal phase gradient on the boundary vanishes—i.e., $N=0$. This can be easily generalized to the case with a known $N \neq 0$ and uniform $\nabla_\perp \Phi \cdot \mathbf{n}$ on the boundary (fine-tuning of the numerical scheme may be needed if we consider nonuniform $\nabla_\perp \Phi \cdot \mathbf{n}$ on the boundary). The generalization can be achieved with the transformations $N_{k-1} \to N_{k-1} - \bar{N}$ and $N_k \to N_k - \bar{N}$ in Eqs.

(15)–(17), where $\bar{N}$ is the known value of N on the boundary.

The diffusion relaxation scheme uses a phase-retrieval method that is not applicable in the case when $I=0$ in the interior, which arises when there are topological defects in the system. However, our aim is to infer the evolution equation of a nonlinear system for which a sufficiently large, and redundant, class of the TDCGL equations is postulated. To achieve this aim, we choose a system in which there are no topological defects. Once the evolution equation of the system is known, one may use the approach outlined in [8] to study the evolution of the system where the phase can be retrieved in the presence of defects.

Finally, we would point out that as was the case in our previous study [9], it is difficult to infer the equation in the presence of noise. It was found that the numerical scheme only works in the case of a very high signal-to-noise ratio—i.e., higher than 10 000:1 for our numerical resolution. Therefore the numerical scheme reported in this paper can only be used when the intensity data is obtained with signal-to-noise ratio higher than 1 part in 10 000.

VIII. CONCLUSION

We have presented a method for "measuring" the evolution equation of a two-dimensional complex wave field obeying the time-dependent complex Ginzburg-Landau equation, given only the modulus information of the wave field. This is done via multiple iterative schemes: one for computing the dissipation function using multiple plane-wave states and another for computing coefficients and functions in the TDCGL equation using localized (noncompact) wave fields. The latter uses a relaxation scheme with a Newton-Raphson-type iteration (termed the modified diffusion algorithm).

Phase retrieval is an important part of the methods to measure the TDCGL equation. The MUDPACK package is employed to retrieve the phase. The rms errors in retrieving the phase is about 5%, with most of the errors occurring at the boundary, where the intensity vanishes. In the presence of diffusion, there is a second-order term in the phase gradient and an iteration method is used to retrieve the phase. The convergence of the iteration scheme is based on the assumption that the second-order term in the phase gradient is smaller than other terms in the equation. For example, for the simulations performed in this paper, the average of the magnitude of the phase gradient is limited to be less than or equal to a value of 1.47.

The iteration phase-retrieval method is embedded in the diffusion relaxation scheme. The diffusion relaxation scheme is based on a known flux metric on the boundary of the localized (noncompact) wave field. Furthermore the present method assumes a smooth phase gradient profile with nonvanishing intensity at all points in the interior of the wave field. In this case we do not allow the presence of topological defects in the wave field. The latter constraint, however, is not a severe limitation of the present method since algorithms exist to retrieve the phase in the presence of topological defects once all parameters and functions in the TDCGL equation are measured using the present method.

The parameters and functions in the TDCGL equation can be inferred accurately. In the present numerical example, the diffusion parameter η and the evolution parameter α can be retrieved within error of 1%, whereas the dissipative and nondissipative interactions are measured to within 2%. The numerical scheme is robust; however, it may be applicable only to data with high signal-to-noise ratio in the modulus information—i.e., higher than 10 000:1 for our numerical resolution. This presently restricts the applicability of our methodology to systems where it is possible to make very accurate measurements on the system.

Notwithstanding the noise problem, this work may be of general significance in a variety of fields, where a model is required to explain the physical phenomenon and make sense of the experimental data.

Knowledge of the evolution equation of a system not only allows us to obtain quantitative understanding and physical insight into the system, but also to study the future evolution of systems where long-term observations are not possible. Future investigations will be directed towards extending the TDCGL model to include gauge fields, which will allow us to describe larger classes of systems including those which exhibit superconductivity.

ACKNOWLEDGMENTS

We acknowledge support from the Australian Research Council (ARC) and the Victorian Partnership for Advanced Computing (VPAC) and useful discussions with Y. Hancock.

APPENDIX A: NUMERICAL METHODS

Here, we give details of the numerical scheme used to infer the TDCGL equation (1) based on the diffusion relaxation scheme discussed in Sec. V A. The diffusion relaxation scheme is given in A 1. Within the diffusion relaxation scheme a Newton-Raphson-type convergence algorithm, given in A 2, has been implemented to modify the diffusion parameter at each iteration. See main text for the definition of symbols used.

1. Diffusion relaxation scheme

- Approximate (or guess) η/α.
- Set iteration number $k=1$.
- Retrieve $\tilde{\Phi}$ at z_1 and z_3 using Eq. (5).
- Solve for α on isointensity surfaces using Eq. (6).
- Calculate N_k (N at the kth iteration).
- Increase η/α by, say 1%.

1. Set $k=k+1$.
2. Retrieve $\tilde{\Phi}$ at z_1 and z_3 using Eq. (5).
3. Solve for α on isointensity surfaces using Eq. (6).
4. Calculate N_k.
5. Use A 2 to find X_{k+1} and $(\eta/\alpha)_{k+1}$.
6. If $|X_{k+1}|>\epsilon$ (a small tolerance), repeat step 1.

- Calculate $f(I)$.

2. Modified diffusion algorithm

IF $N_k N_{k-1} < 0$ THEN

$$X_{k+1} = -\frac{N_k}{N_k - N_{k-1}} X_k$$

ELSE
IF $|N_k| > |N_{k-1}|$ THEN

$$X_{k+1} = -\frac{N_k}{N_{k-1}} X_k$$

ELSE

$$X_{k+1} = \frac{N_k}{N_{k-1}} X_k$$

END IF
END IF

$$\left(\frac{\eta}{\alpha}\right)_{k+1} = (1 + X_{k+1})\left(\frac{\eta}{\alpha}\right)_k$$

3. Numerical scheme for inferring the TDCGL equation

The numerical scheme used to infer the TDCGL equation assumes that we have prepared multiple plane-wave states $P(I_n)$ and a noncompact localized state $L(I)$ (see Sec. V C for the definition of the notation used). The scheme proceeds as follows:

- Approximate (or guess) η/α denoted by $\tilde{\eta}/\alpha$.
1. Use $\tilde{\eta}/\alpha$ to infer the dissipation $g(I_n)/\alpha$ for each I_n.
2. Transform $g(I_n)/\alpha$ to $g(I)/\alpha$ and then to $g_L(x,y)/\alpha$.
3. Use $\tilde{\eta}/\alpha$, $g_L(x,y)/\alpha$, and A 1 to find $\tilde{\Phi}$, α, and η/α.
4. If $|\eta/\alpha - \tilde{\eta}/\alpha| < (\tilde{\eta}/\alpha)\epsilon'$, let $\tilde{\eta}/\alpha = \eta/\alpha$; go to 1.

- Calculate $f(I)$.

[1] *Chaos and its Reconstruction*, edited by G. Gouesbet, S. Meunier-Guttin-Cluzel, and O. Menard (Nova Science Publisher, New York, 2003).
[2] O. Nelles, *Nonlinear System Identification* (Springer, Berlin, 2001).
[3] H. Voss, M. J. Bünner, and M. Abel, Phys. Rev. E **57**, 2820 (1998).
[4] M. Bär, R. Hegger, and H. Kantz, Phys. Rev. E **59**, 337 (1999).
[5] P. Le Gal, J. F. Ravoux, E. Floriani, and T. Dudok de Wit, Physica D **174**, 114 (2003).
[6] D. M. Paganin and K. A. Nugent, in *Advances in Imaging and Electron Physics*, edited by P. W. Hawkes (Harcourt, Kent, 2001), Vol. 118, p. 85.
[7] M. R. Teague, J. Opt. Soc. Am. **73**, 1434 (1983).
[8] Y.-R. E. Tan, D. M. Paganin, R. P. Yu, and M. J. Morgan, Phys. Rev. E **68**, 066602 (2003).
[9] R. P. Yu, D. M. Paganin, and M. J. Morgan, Phys. Lett. A **341**, 156 (2005).
[10] I. S. Aranson and L. Kramer, Rev. Mod. Phys. **74**, 99 (2002).
[11] L. J. Allen and M. P. Oxley, Opt. Commun. **199**, 65 (2001).
[12] B. E. A. Saleh and M. C. Teich, *Fundamentals of Photonics* (Wiley, New York, 1991).
[13] N. N. Akhmediev and A. Ankiewicz, *Solitons, Nonlinear Pulses and Beams* (Chapman and Hall, London, 1997).
[14] L. Pitaevskii and S. Stringari, *Bose-Einstein Condensation* (Oxford University Press, Oxford, 2003).
[15] L. M. Pismen, *Vortices in Nonlinear Fields* (Oxford University Press, Oxford, 1999).
[16] D. L. Feder and C. W. Clark, Phys. Rev. Lett. **87**, 190401 (2001).
[17] E. Madelung, Z. Phys. **40**, 322 (1926).
[18] P. Wesseling, *An Introduction to Multigrid Methods* (John Wiley & Sons, Chichester, 1992).
[19] J. Adams, Appl. Math. Comput. **34**, 113 (1989).
[20] J. Adams, Appl. Math. Comput. **53**, 235 (1993).
[21] http://www.scd.ucar.edu/css/software/mudpack
[22] T. E. Gureyev, A. Roberts, and K. A. Nugent, J. Opt. Soc. Am. A **12**, 1932 (1995).
[23] M. H. Anderson *et al.*, Science **269**, 198 (1995).
[24] C. C. Bradley, C. A. Sackett, J. J. Tollett, and R. G. Hulet, Phys. Rev. Lett. **75**, 1687 (1995).
[25] K. B. Davis, M. O. Mewes, M. R. Andrews, N. J. van Druten, D. S. Durfree, D. M. Kurn, and W. Ketterle, Phys. Rev. Lett. **75**, 3969 (1995).
[26] E. M. Lifshitz and L. P. Pitaevskii, *Statistical Physics* (Butterworth-Heinemann, Stoneham, MA, 1980).
[27] W. H. Press, S. A. Teukolsky, W. T. Vetterling, and B. P. Flannery, *Numerical Recipes in FORTRAN*, 2nd edition (Cambridge University Press, Cambridge, 1992).
[28] E. R. Tracy and H. H. Chen, Phys. Rev. A **37**, 815 (1988).
[29] F. Kh. Abdullaev, S. A. Darmanyan, S. Bischoff, and M. P. Sorensen, J. Opt. Soc. Am. B **14**, 27 (1997).